A Study of Bubble Wetting on Surfaces

by

Julia Katherine Day

Submitted to the Department of Mechanical Engineering in partial fulfillment of the requirements for the degree of

Bachelor of Science in Engineering as Recommended by the Department of Mechanical Engineering

at the

MASSACHUSETTS INSTITUTE OF TECHNOLOGY

June 2010

Author .....

Department of Mechanical Engineering
May 10, 2010

Certified by.....

Kripa Varanasi
Assistant Professor
Thesis Supervisor

Accepted by.....

John H. Lienhard V
Collins Professor of Mechanical Engineering
Chairman, Undergraduate Thesis Committee

A Study of Bubble Wetting on Surfaces

by

Julia Katherine Day

Submitted to the Department of Mechanical Engineering
on May 10, 2010, in partial fulfillment of the
requirements for the degree of
Bachelor of Science in Engineering as Recommended by the
Department of Mechanical Engineering

Abstract

In microfluidics, the formation of bubbles within devices obstructs flow and can damage the microfluidic chip or the samples contained therein. This thesis works toward a better understand of bubble wetting on surfaces, so that future microfluidics devices can be designed to be more robust and free of bubbles. Current wetting theory as applied to bubbles is examined, and two key areas for improvement are identified: disjoining pressure effects and gravitationaleffects. Wetting of textured surfaces is also analyzed for bubble application, leading to a prediction that a model based on a Cassie-Baxter analysis with knowledge of bubble wetting on a flat surface would be most accurate compared to other models. Dynamic and sessile bubble contact angles and droplet contact angles were measured on smooth acrylic, fluorosilanized silicon, glass, nylon, and silicon. These results were compared to the existing model, and the resulting error showed a strong correlation with a Pearson's correlation coefficient of 0.863 to the magnitude of the bubble contact angle hysteresis. Because contact angle hysteresis can be related to the disjoining pressure, these results were a good indicator that disjoining pressure should be considered in developing improved bubble wetting models. Dynamic and sessile bubble contact angles and droplet contact angles were also measured on four silicon samples with different surface textures. These results were compared to three existing wetting models as applied to bubble wetting, and it was found that the Cassie-Baxter model based on the bubble contact angle on a smooth silicon surface was most accurate, with an average percentage error of 0.8%. Finally, recommendations for further research to support developing models of bubble wetting are made.

Thesis Supervisor: Kripa K. Varanasi

Title: Assistant Professor

Contents

List of Figures

List of Tables

Chapter 1

Introduction

1.1 Applications

The study of microfluidics devices has become increasingly popular over the past twenty years for a variety of applications (Whitesides 368). These applications range from possible cooling chips for computers to DNA sequencing chips to laboratory testing of fluid mechanics (370-372). However, there exists a problem that any engineer working with microfluidics devices will encounter in her career: bubbles. Whether from evaporation within a channel, or from faulty sealing, a bubble lodged within a microfluidics chip can produce hours of frustration and can possibly damage samples. Methods to clear a microfluidics device of bubble include increasing inlet pressure and physically disturbing the chip near the area of the bubble.

Especially as microfluidic devices become more complicated, for example as in Figure 1.1.1, this problem only becomes more prevalent. Reliability is a fundamental criterion for good design, especially considering that for applications like analyzing forensic DNA evidence, there is only a limited sample available and contamination means complete failure. Thus, a better understanding of how and why bubbles wet themselves onto surfaces could help microfluidics engineers design better chips that prevented bubbles adhesion and increased the reliability of their devices.

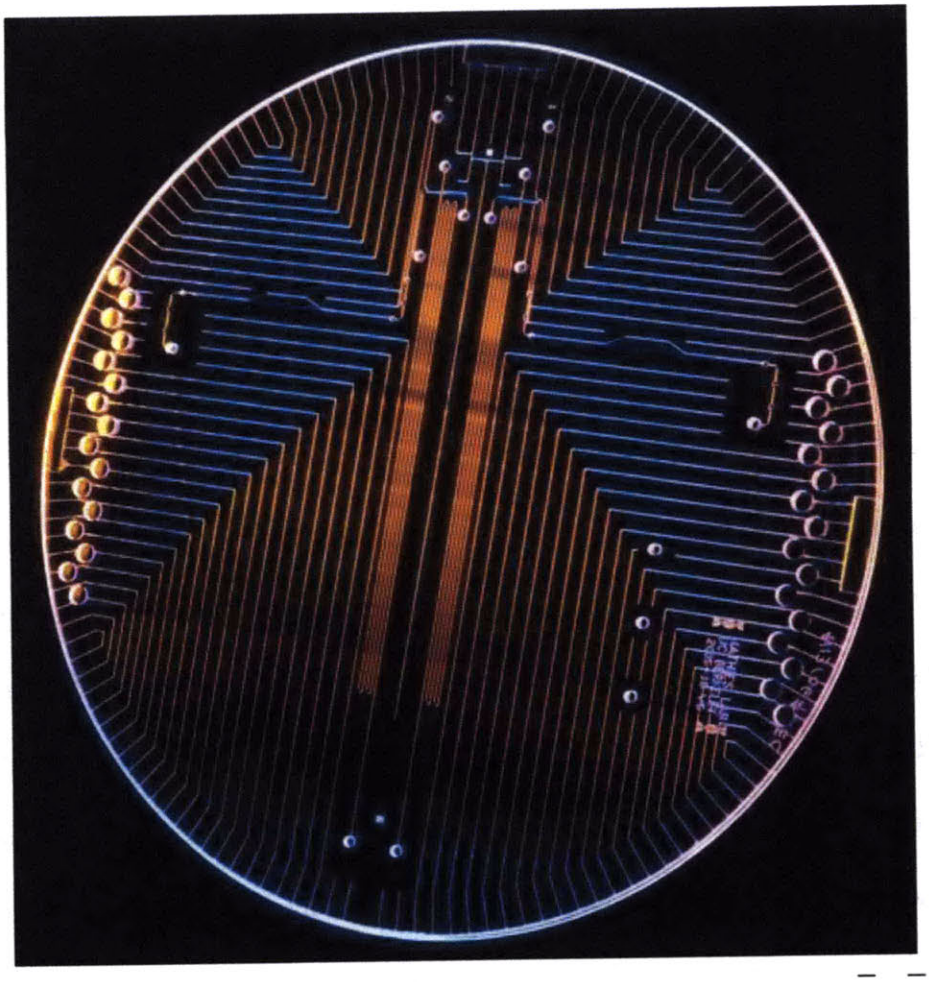

Figure 1.1.1 A microfluidics chip used for DNA analysis (Mathies Lab).

1.2 Objectives

This thesis will attempt to further develop methods for predicting the wetting of a bubble on both flat and textured surfaces. The current droplet and trapped bubble wetting theory that drives current knowledge about bubble wetting, including current limitations of understanding, is explained in Chapter 2.

The current theories for predicting bubble wetting are analyzed in Chapter 3. It is predicted that disjoining pressure effects and gravitational effects will cause significant

differences between experimentally determined bubble wetting and the bubble wetting predicted using the current method based on droplet wetting. For textured surfaces, Cassie-Baxter and Wenzel regimes are discussed and used to further an analysis of the best method to predict the wetting of a bubble. This paper predicts that the most accurate method is based on the bubble wetting of a flat surface of the same material.

Wetting experiments are then performed to test these hypotheses in Chapter 4. Bubbles are adhered to five different flat surfaces: acrylic, fluorosilanized silicon, glass, nylon and silicon dioxide and the static and dynamic contact angles were measured with a goniometer. The same experiments were then performed on four samples of textured silicon with different critical aspect ratios. Static contact angle measurements were also performed on all aforementioned surfaces. The experimental results are then compared to predictions from Chapter 3. Finally, conclusions and recommendations are made in Chapter 5.

Chapter 2

Wetting Theory

2.1 Wetting and the Contact Angle

In the study of wetting phenomena, an important and useful parameter used to quantify the extent of wetting is the contact angle. Considering the case of a sessile water droplet on a surface in ambient air, it is clear that it is a three phase system with a solid surface, a fluid and a vapor. The line along the solid surface where all three phases meet is the contact line. The contact angle, therefore, is defined as the apparent angle between the solid-liquid interface and the liquid-vapor interface at the contact line, as shown in Figure 2.1.1.

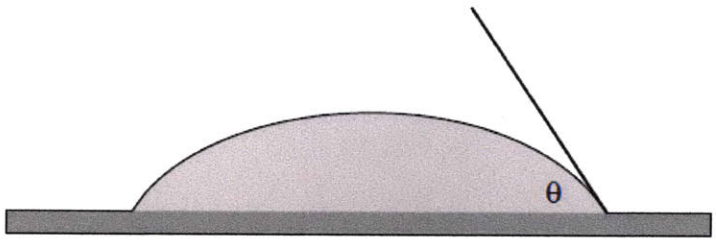

Figure 2.1.1 An illustration of the contact angle of a droplet on a surface (Radke et.al. 3).

Furthermore, for each of these pairs of phases there is a separate interface at the boundary between the two phases, creating three interfacial surfaces in the system. At each of the interfacial surfaces, there exists an interfacial tension γ, sometimes referred to as a surface tension. This interfacial tension occurs because, as illustrated in Figure 2.1.2, molecules at the surface have fewer bonds with neighboring molecules (de Gennes et.al. 2-3). Because of course

the A molecules do not bond as well with the neighboring B molecules as they do with their own bulk materials (otherwise mixing would be the rule and the boundary would no longer exist), the surface molecules have fewer total bonds than the molecules in the bulk region. This relative lack of bonding means that the molecules at the surface have excess internal energy, U (Miller and Neogi 11-13). Thus, the interfacial tension is defined as the change in internal energy required to sustain an additional unit area dA of interfacial surface for a constant number of moles of each species in the interfacial region:

$$\gamma = \left(\frac{dU}{dA}\right)_{surface} \tag{2.1.1}$$

Thus, a larger area requires more energy to sustain, and the existence of an interfacial tension generally drives the system to minimize interfacial surface area.

In the case of case of liquid-vapor interfaces, it can be deduced that the optimal shape for a droplet or bubble in the absence of gravity would be a sphere. For a more general case of a curved interfacial surface, the Laplace equation shows that the mean curvature on the surface, H is constant for any point on the surface:

$$\Delta P = \gamma_{LV} H \tag{2.1.2}$$

where H is defined by the two principle radii of the interfacial surface R_1 and R_2 as

$$H = \left(\frac{1}{R_1} + \frac{1}{R_2}\right), \tag{2.1.3}$$

ΔP is defined as the pressure difference between the liquid and the vapor, and γ_{LV} is the interfacial tension between the liquid and the vapor (9-10). The Laplace equation also shows that the pressure inside a bubble or droplet is necessarily larger than the pressure outside because the curvature relative to the inside is positive and that this pressure difference decreases when the size of the droplet or bubble increases.

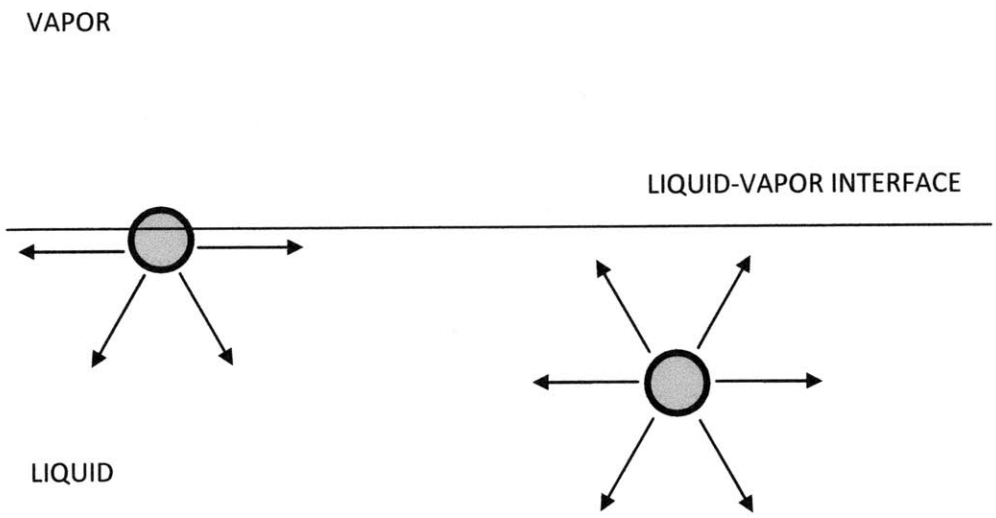

Figure2.1.2 An illustration adapted from de Gennes et.al. that shows how the molecule on the left, which is at the surface of the liquid, experiences less attractive interactions that the molecule on the right, which is within the bulk of the fluid (2).

When a liquid wets a surface, the process simultaneously replaces an equal area of liquid-vapor interface and solid-vapor interface with the newly created solid-liquid interface. This is expressed in the Dupré equation (Miller and Neogi 65), which defies the work of cohesion between the liquid and solid interface, W_{SL} as follows

$$W_{SL} = \gamma_{SV} + \gamma_{LV} - \gamma_{SL}. \tag{2.1.4}$$

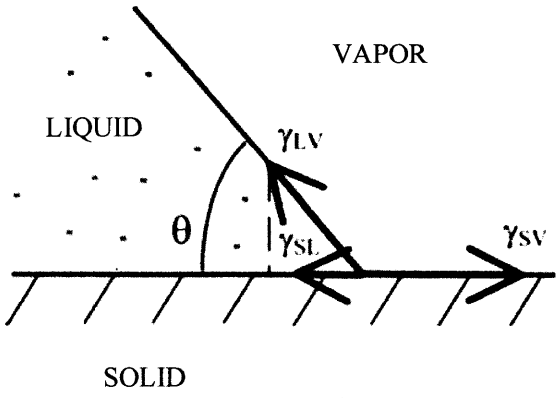

Figure 2.1.3 A close-up view of the three phase interface adapted from Bhushan and Nosonovsky (74).

Another important relation in wetting is Young's equation, which relates the three interfacial tensions to the contact angle:

$$\gamma_{SV} = \gamma_{SL} + \gamma_{LV} \cos\theta \tag{2.1.5}$$

where γ_{SV}, γ_{SL}, and γ_{LV} are the interfacial tensions between the solid and vapor, the solid and liquid, and the liquid and vapor respectively; and θ is the contact angle (Miller and Neogi 61). It should also be noted that combining Equations 2.1.4 and 2.1.5 results in the Young- Dupré equation:

$$W_{SL} = \gamma_{LV}(1 + \cos\theta). \tag{2.1.6}$$

Although Young's equation can also be proven in a more rigorous fashion than will be attempted in this paper, it is apparent from Figure 2.1.2 that a simple force balance will lead to the same relation assuming that gravity effects are negligible (61-63). From this equation, it is clear that there are three important regimes, first where $\cos(\theta)$ is less than -1, second where $\cos(\theta)$ is greater than 1 and third where $\cos(\theta)$ is between -1 and 1. In the first case, the liquid and surface do not adhere at all, and in the second case the liquid achieves complete adsorption with the surface. The last case is the most interesting case, where the liquid is neither completely rejected

nor completely absorbed by the surface. In general, a contact angle for a water droplet greater than 90 degrees is referred to as hydrophobic and a contact angle less than 90 degrees is hydrophilic. The categories of superhydrophobic and superhydrophilic are reserved for surfaces that achieve a contact angle of greater than 150 degrees and less than 10 degrees, respectively (Bhushan and Nosonovsky 81-82).

The magnitude of the interfacial tensions is driven by molecular bonding, such as Van der Waals effects, between the different phases and within each bulk phase, and in depth explanations are outside the scope of this paper. However, it has been shown that interfacial tensions are temperature dependent, as can be seen in Table 2.1.1. Cini et.al. performed experiments to determine the interfacial tension of water and air at different temperatures using the equilibrium ring method, which related the force required to pull a platinum ring out of a water bath to the interfacial tension of water and air.

Table 2.1.1 Results from Cini et.al. show the temperature dependence of the surface tension of water. The left column gives the measured temperature and the right column shows the measured surface tension of water at each temperature, γ_T, normalized by the surface tension of water at 20°C, γ_{20} (291).

T (°C)	γ_T/γ_{20}
5.15	1.02950
9.67	1.02076
15.04	1.01008
20.07	0.99986
25.00	0.98970
30.20	0.97866
35.24	0.96799

2.2 Dynamic Contact Angle

In addition to measuring the contact angle of a static contact line, it is also possible to observe the contact angle of moving contact lines. With droplets, it is increasingly common to measure the advancing and receding contact angles in addition to the sessile contact angle. The advancing contact angle, θ_{adv}, is measured when the volume of the droplet is increasing and in the process of wetting more surface whereas the receding contact angle, θ_{rec}, is measured when the volume of the droplet is decreasing and in the process of dewetting the surface. It is well known that there exists what is known as the contact angle hysteresis between the receding and advancing contact angles, which reflects the thermodynamic irreversibility inherent in wetting and dewetting (Radke et.al. 90-91). Accordingly, the more "friction" inherent to a surface, whether that be surface contaminants or surface roughness, the higher the resulting contact angle hysteresis tends to be. However, even with atomically smoothed surfaces, the smallest contact angle hysteresis that has been observed was non-zero, though less than 1 degree (91).

The presence of surface imperfections also causes a local tilt to the surfaces, which will change the observed contact angle of a droplet or surface. Many studies have shown that because of this, there is in fact no one contact angle for a given surface (91). Furthermore, it is nearly impossible to remove all dynamic effects when measuring a sessile drop because in addition to vibratory disturbances, evaporation can produce dynamic effects on this size scale, so the history of the droplet can affect the contact angle (297-299 Bhushan and Nosonovsky). Thus, because there is always microscopic motion at the contact line, the static contact angle is not truly static,

and so the observed contact angle should stabilize between the advancing and receding contact angle and this hypothesis has been borne out in the literature (297).

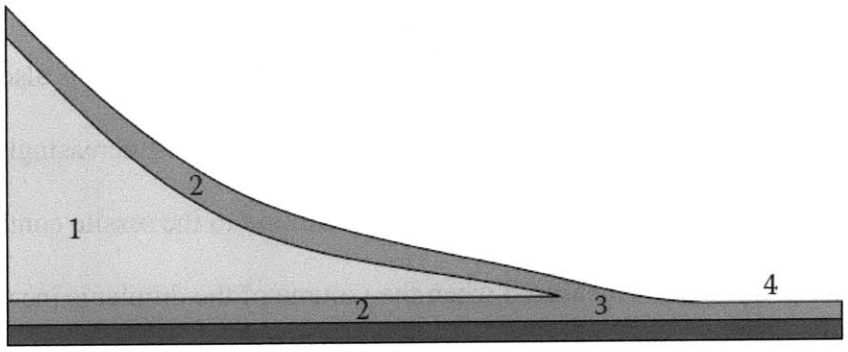

Figure 2.2.1 An illustration of the boundary layer at the three phase interface (Radke et.al. 13).

It is also important to explain that at the microscopic level, on the scale of 0.1 μm to be exact, there exists a boundary layer at the contact line of a droplet on a surface, as illustrated in Figure 2.2.1 (Radke et.al. 13). This boundary layer exists at the contact line and extends radially outward in a very thin layer of water, and is the result of surface forces. The amount of surface force per unit area is known as the disjoining pressure, although it can act as either a repellant or attractive pressure between two surfaces (de Gennes et.al. 88-90). The three main surface forces that create the disjoining pressure are Van der Waals forces, electrokinetic forces, and structural forces (especially for molecules that are electric dipoles, like water) (Radke et.al.13-16). Radke et.al. showed that the disjoining pressure is related to the contact angle hysteresis in the following equation

$$\cos\theta - \cos\theta_a = 1 - \frac{1}{\gamma_{LV}}\left[P_s h_s - P_a h_a + \int_{h_s}^{h_a} \Pi(h)dh\right] \qquad (2.2.1)$$

where P_s is the pressure difference between the liquid and the vapor for a sessile droplet, P_a is the pressure difference between the liquid and the vapor for the advancing droplet, h_s is the height of

the film, h_a is the height of the film, and $\Pi(h)$ is the disjoining pressure as a function of h. The same derivation can be carried out to prove a corollary equation

$$\cos\theta_r - \cos\theta_a = 1 - \frac{1}{\gamma_{LV}}\left[P_r h_r - P_a h_a + \int_{h_r}^{h_a} \Pi(h)dh\right] \tag{2.2.2}$$

where P_r is the pressure difference between the liquid and the vapor for the receding droplet and h_r is the height of the film (305).

2.3 Effects of Roughness and Surface Texture on Wetting

In addition to affecting contact angle hysteresis above in Section 2.2, roughness has further fundamental effects on wettability that will be explained in this section. For a given flat projected area A_F, roughness increases total surface area A. This is the basis of the Wenzel model

$$\cos\theta = R_f \cos\theta_0 \tag{2.3.1}$$

where θ is the contact angle of the rough surface, θ_0 is the contact angle of the idealized smooth surface and R_f is the ratio of the total surface area to the total surface area the flat projected area

$$R_f = \frac{A}{A_F}, \tag{2.3.2}$$

which is defined as the dimensionless surface roughness factor (Bhushan and Nosonovksy 86). Because R_f is by definition greater than or equal to 1, it is clear from Equation 2.3.1 that roughness will decrease the contact angle of a hydrophilic surface and will increase the contact angle of a hydrophobic contact angle, so roughness can be said to enhance the wetting or non-wetting properties inherent to a surface.

A similar analysis can give the results for a heterogeneous surface composed of two separate materials. Given a surface with a fractional area f of a material with contact angle θ_1, and a fractional area 1-f of a material with contact angle θ_2, it is possible to derive the Cassie equation:

$$\cos\theta = f\cos\theta_1 + (1-f)\cos\theta_2 \tag{2.3.3}$$

where θ is the contact angle of the heterogeneous surface (86-87). The Cassie-Baxter equation gives the special result of the Cassie equation where the heterogeneous surface is comprised of a solid component with a fractional area f_{SL} and a vapor component with a fractional area 1-f_{SL}, as with a solid with air pockets:

$$\cos\theta = f_{SL}\cos\theta_{SL} + (1-f_{SL})\cos\theta_{LV} \tag{2.3.4}$$

Considering that the contact angle where the liquid does not wet a surface is entirely non-wetting, we can take the contact angle of the liquid-vapor interface to be 180 degrees, which simplifies the equation to

$$\cos\theta = f_{SL}\cos\theta_{SL} - 1 + f_{SL} \tag{2.3.5}$$

and then combining the above equation with the Wenzel equation gives the true Cassie-Baxter equation:

$$\cos\theta = R_f f_{SL}\cos\theta_{SL} - 1 + f_{SL}. \tag{2.3.6}$$

These equations also lead to the popular categorizations of the Wenzel and Cassie-Baxter regimes with describe two separate possible states of wetting for rough surfaces. In the Wenzel regime, the cavities in a rough surface are wetted and in the Cassie-Baxter regime the cavities in a rough surface are not wetted but are instead filled with vapor. The differences between these two wetting regimes are shown in Figure 2.3.1.

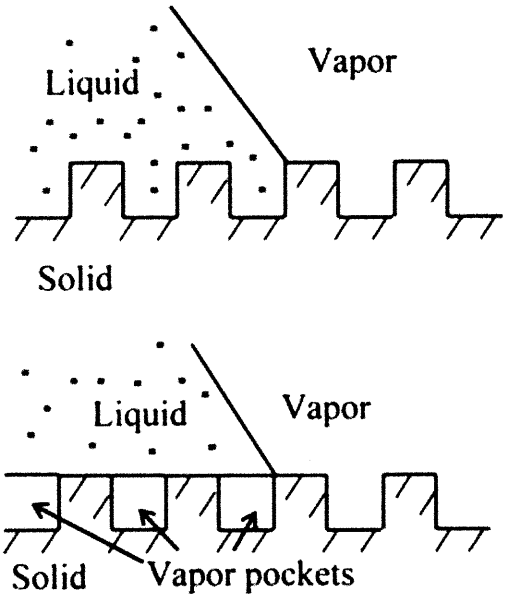

Figure 2.3.1 The top illustration shows the Wenzel wetting regime where liquid penetrates the cavities. The lower illustration depicts the Cassie-Baxter regime where the cavities are instead filled with vapor and the liquid rests on top of the surface formed by the solid and the vapor pockets (83).

2.4 Limits of Wetting Theory

The contact angle commonly observed by the naked eye or goniometers in experiments is sometimes referred to as the apparent contact angle because it is a relatively macro-scale parameter compared to the contact angle observed at the micro- or nano-scale. This phenomenon was documented by Salmeron and Xu in their Scanning Polarization Force Microscopy (SPFM) experiments imaging nano-droplets and measuring the contact angle. They found that for as the droplet height approached zero, so did the contact angle (7212-7214). As the droplet height increased, the contact angle quickly approached the macro contact angle, as shown in Figure 2.4.1. Current theory suggests that this phenomenon is related to the disjoining pressure effects (Radke et.al. 74). Figure 2.4.2 shows an illustration of how this precursor film also has its own contact angle, which is much smaller than the apparent contact angle.

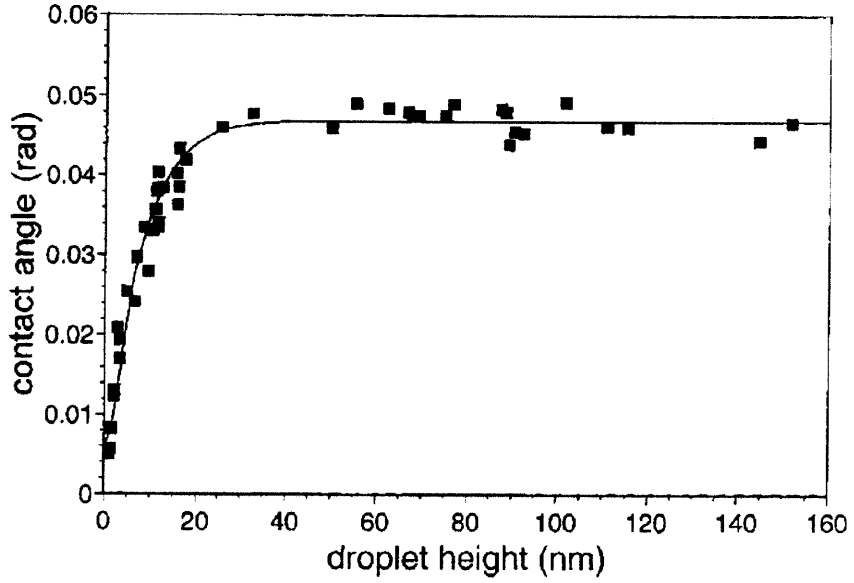

Figure 2.4.1 In this plot of contact angle over droplet height adapted from Salmeron and Xu, the results from SPFM measurements of the contact angle of nano-droplets of glycerol condensated onto mica compared to the droplet height (7213).

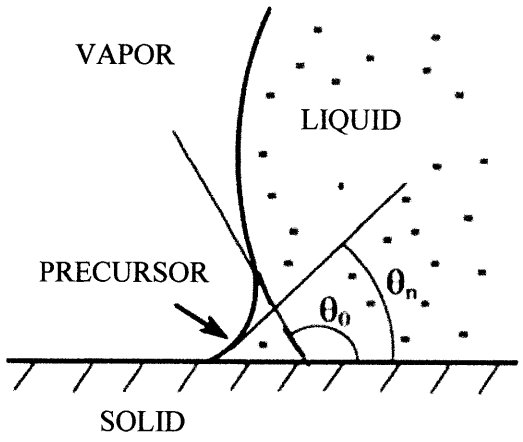

Figure 2.4.2 An illustration adapted from Radke et.al. which shows the difference between the apparent or macro contact angle, here labeled θ_0, and the micro-/nano-scale precursor contact angle, which is labeled θ_n (75).

Figure 2.4.3 Adapted from Feng et.al., the droplet on the left shows a water droplet adhered to a sample of rose petal. From this image, it is clear that the contact angle is within the superhydrophobic range of >150 degrees. The droplet on the right is a water droplet on the same sample of rose petal now inverted to show that the droplet does not roll off the rose petal even when upside-down (4115).

Furthermore, it has been shown that a large contact angle and high adhesion can between a water droplet and a surface can indeed coexist. Feng et.al. tested the wetting properties of rose petals and show in Figure 2.4.3 that although the contact angle was larger than 150 degrees, the droplet remained attached to the surface even when the system was upside down and in fact never rolled off. As with the lotus leaf, these amazing properties were greatly attributed to the hierarchical structure on the surface of the rose petal, though of course to different effect. The authors explained that whereas the lotus leaf induces a Cassie state where water can neither impregnate the larger grooves nor the smaller grooves on the surface, the rose petal induces a Cassie impregnating wetting state where water could impregnates the larger grooves on the surface but not the smaller, as shown in Figure 2.4.4 (4115-4117).

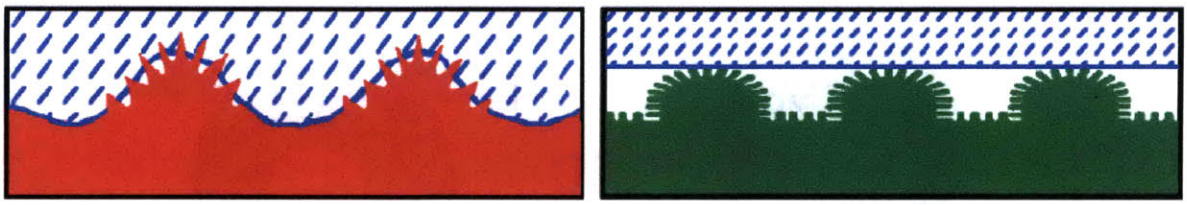

Figure 2.4.4 This illustration from Feng et.al. shows the theoretical wetting regimes of the rose petal on the left and the lotus leaf on the right. Water on the rose petal is in an impregnating wetting state where the larger cavities are filled with water but not the smaller cavities. Water on the lotus leaf is in a true Cassie-Baxter state where both large and small cavities are filled with air while the water rests on top (4117).

Chapter 3

Predicting the Bubble Wettability of a Surface

3.1 Smooth Surface Analysis

Given a bubble attached to a solid surface submerged in water, it is possible to perform a three phase system analysis with Equation 2.1.4 that is directly analogous to the droplet analysis performed in Section 2.1. Whereas before analysis focused on the work of cohesion between the solid and the liquid, W_{SL}, now it will focus on the work of cohesion between the solid and the vapor, W_{SV}. Just as before the liquid-solid interface replaced a liquid-vapor and solid-vapor interface of the same area, now a solid-vapor interface replaces liquid-solid and liquid-vapor interface such that

$$W_{SV} = \gamma_{SL} + \gamma_{LV} - \gamma_{SV} \tag{3.1.1}$$

where γ_{SL}, γ_{LV}, and γ_{SV} are the interfacial tensions at the liquid-solid interface, the liquid-vapor interface and the solid-vapor interface, respectively.

Continuing with Equation 2.1.5, a force balance analysis of the bubble system in Figure 3.1.1 reveals the Young equation for a bubble:

$$\gamma_{SL} = \gamma_{SV} + \gamma_{LV} \cos\theta_{bubble} \tag{3.1.2}$$

where θ_{bubble} is the contact angle of the bubble and the effects of gravity are ignored. Thus, it follows that the Young-Dupré equation for the bubble is

$$W_{SV} = \gamma_{LV}(1 + \cos\theta_{bubble}). \tag{3.1.4}$$

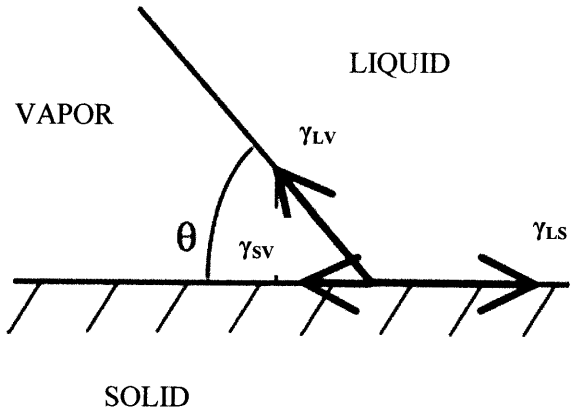

Figure 3.1.1 A close-up view of the three phase interface adapted from Bhushan and Nosonovsky (74). The same image as Figure 2.1.3 with the vapor and liquid reversed.

To relate the contact angle of the bubble system to the contact angle of the droplet system with the same vapor, liquid solid and therefore the same interfacial tensions, Equation 2.1.5 and Equation 3.1.2 are recombined to show

$$\gamma_{SL} = \gamma_{SL} + \gamma_{LV}\cos\theta + \gamma_{LV}\cos\theta_{bubble} \tag{3.1.5a}$$

$$\gamma_{LV}\cos\theta = -\gamma_{LV}\cos\theta_{bubble} \tag{3.1.5b}$$

$$\theta = 180 - \theta_{bubble} \tag{3.1.5c}$$

where θ is the contact angle of the droplet and both contact angles are measured in degrees.

The relation between the work of adhesion between the two systems can also be determined, by combining Equation 3.1.4 with Equation 3.1.5c.

$$W_{SV} = \gamma_{LV}(1 - \cos\theta) \tag{3.1.6}$$

then substituting in Equation 2.1.6 shows

$$W_{SV} = W_{SL} - 2\,\gamma_{LV}\cos\theta. \tag{3.1.7}$$

Thus, for a hydrophilic surface, the value of $\cos\theta$ will be positive, and so the work of adhesion between the solid-vapor interface will be smaller than that of the solid-liquid interface and the opposite will be the case for a hydrophobic surface.

3.2 Rough and Textured Surface Analysis

Reintroducing the roughness factor R_f and Equation 2.3.1 from Section 2.3, Equation 3.1.5b becomes

$$\gamma_{LV} R_f f \cos\theta = -\gamma_{LV} R_f \cos\theta_{bubble} \tag{3.2.1}$$

so Equation 3.1.5c still holds and roughness should have no effect on the relation between the trapped bubble contact angle as compared the droplet contact angle. However, this analysis assumes that the droplet and bubble are both in the Wenzel regime, that both the bubble and the droplet have completely wetted the surface.

In the Cassie regime, Equation 2.3.6 becomes

$$\cos\theta_{bubble} = R_f f_{top} \cos\theta_{SV} - 1 + f_{top} \tag{3.2.2a}$$

substituting in a rearranged Equation 2.3.6 as shown below

$$\cos\theta - R_f f_{top} \cos\theta_{SL} = -1 + f_{top} \tag{3.2.2b}$$

results in

$$\cos\theta_{bubble} = f_{top} \cos\theta_{SV} + \cos\theta - f_{top} \cos\theta_{SL} \tag{3.2.2c}$$

$$\cos\theta_{bubble} = R_f f_{top} (\cos\theta_{SV} - \cos\theta_{SL}) + \cos\theta \tag{3.2.2d}$$

Equation 3.2.2d gives a relation between the bubble contact angle and the droplet contact angle assuming that both systems were in a Cassie state on the same surface. However, it is clear from 3.1.5c that a surface that resulted in a water droplet that achieved a completely wetting Wenzel state would likely result in a bubble that achieved the non-wetting Cassie state instead of

the Wenzel state. Thus, a more accurate prediction of bubble contact angle on a textured surface would probably be determined from the bubble contact angle on a flat surface as opposed to using either model for predicting the bubble contact angle based on the droplet contact angle.

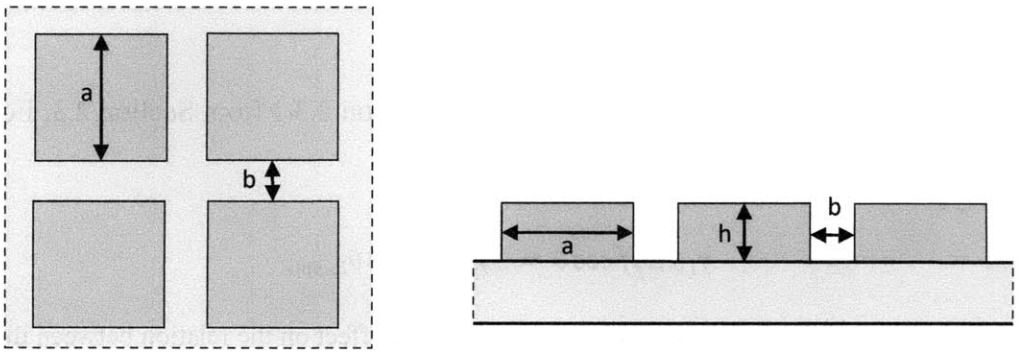

Figure 3.2.1 An illustration showing the critical dimensions *a,b,* and *h* for a textured surface made of raised squares. The left shows a top-down view of the surface and the right shows an image of the surface from the side.

A microtextured surface presents an easily quantifiable method of establishing roughness and heterogeneity parameters. It is possible to calculate R_f for a surface textured with raised squares with dimensions given in Figure 3.2.1 [forthcoming]. A formula for unit total area is given below

$$A = (a + b)^2 + 4ha \tag{3.2.4}$$

and a unit of projected area is

$$A = (a + b)^2 \tag{3.2.5}$$

so it follows from Equation 2.3.2 that the roughness factor R_f is

$$R_f = \frac{(a+b)^2+4ha}{(a+b)^2}. \tag{3.2.6}$$

Futhermore, the quantity f is determined by calculating the percentage of the projected area that constitutes the top surface

$$f = \frac{a^2}{(a+b)^2}. \tag{3.2.7}$$

3.3 Disjoining Pressure Effects

Of course, so far all analysis has assumed that a trapped bubble can be treated essentially the same as a droplet, which is not truly the case. A major difference in wetting mechanisms for a droplet and a bubble is connected to the disjoining pressure. In a droplet, disjoining pressure effects result in a precursory water film that protrudes radially from the droplet in on the surface. This section will predict how disjoining pressure effects will affect bubble wetting. As mentioned in Section 2.2, the magnitude of the disjoining pressure is related to Van der Waals forces, electrokinetic forces, and structural forces caused by the build-up polar molecules. On all three measures, water, which is denser, a better conductor and composed of polar molecules, clearly outstrips air. Thus, just as even in a droplet system with a hydrophobic surface there exists a precursory water film, this analysis predicts that in the bubble system there will be a thin water film at the edge of the bubble between the air and the surface that will interfere with bubble wetting.

The extent to which it affects bubble wetting can be predicted using Equation 2.2.2. Assuming droplets and bubbles of equal sizes, P_r and P_a should be the same, and of course assuming a water-air-surface system, γ_{LV} will be the same for all cases. Assuming that with the same contact line velocity, the critical heights h_r and h_a are constant, Equation 2.2.2 simplifies to

$$\cos\theta_r - \cos\theta_a = C_1 + C_2K \tag{3.3.1}$$

where C_1 and C_2 are both constants related to the aforementioned system constants and K is a measure of the magnitude of the disjoining pressure effects. This simplified relation more clearly shows that there is a relationship between the magnitudes of the hysteresis of the system and the disjoining pressure effects.

3.4 Gravitational Effects

Although the shape of a trapped bubble is usually assumed to be the mirror image of a droplet on a surface, this section will examine this assumption in further detail. Working from that assumption, this section will examine a droplet and a trapped bubble of equal size and shape. Because of gravitational effects, in both the fluid and the vapor, the density of the material changes with the position along the z axis. Thus, there is more mass in the bottom of the droplet and bubble, which shifts the centers of mass such that the center of mass of the bubble will be farther from the surface and the center of mass of the droplet is closer to the surface. A curved surface analysis is dependent on the location of center of mass, so because that variable changes, so too must the shape of the droplet. This difference could also have an effect on the relationship between the contact angles of a trapped bubble and a droplet on the same surface.

3.5 Chapter Summary

In this chapter, current wetting theory was explored to find relations that could help to predict bubble wetting. Young's equation, the Wenzel equation and the Cassie-Baxter equation were all developed to explore the relationship between bubble and droplet contact angle in multiple wetting regimes. It was determined that near the Cassie and Wenzel states on textured surface, a prediction of bubble contact angle would be less accurate if based on the droplet contact angle instead of the bubble contact angle on a flat surface. Roughness and heterogeneity equations were put forth for surfaces textured with raised squares. Disjoining pressure and gravity effects were introduced as possible sources of need for a correction factor. Equation 3.3.1

was derived to show the relation between disjoining pressure effects and the magnitude of contact angle hysteresis.

Chapter 4

Testing Bubble and Droplet Wetting

4.1 Experimental Set-up

The goniometer system in Figure 4.1.1 was used to measure the contact angles of the droplets and bubbles in all experiments. A camera was used to take images of the sample, and these images were then semi-automatically processed using DropImage software. After the substrate surface line and inner bounds of the droplet or bubble had been selected, as shown in Figure 4.1.2, DropImage software then computed and recorded the contact angle for each side of the droplet or bubble.

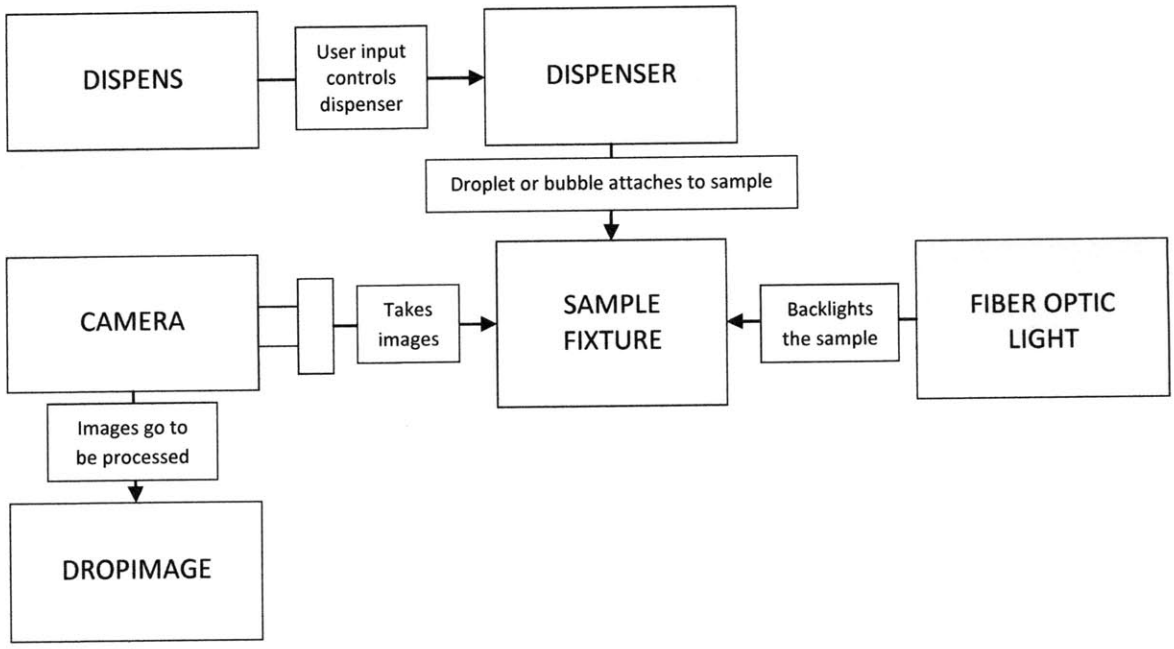

Figure 4.1.1 An illustrated schematic of the goniometer system used to make contact angle measurements.

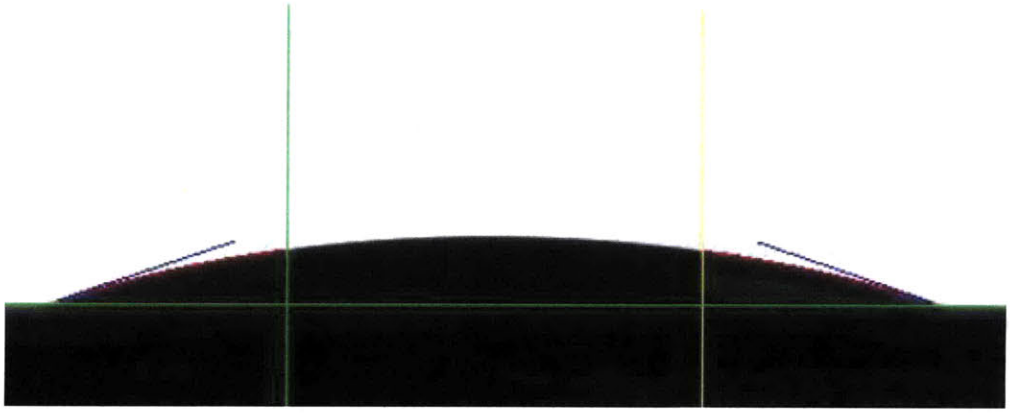

Figure 4.1.2 A still image from DropImage software, showing how the GUI works. The user places the vertical green line to the right of the left contact angle and the yellow vertical line to the left of the right contact angle. The user also places the surface line, the green horizontal line. The software then determines the surface curvatures, shown in red, and the contact angles, shown with blue lines.

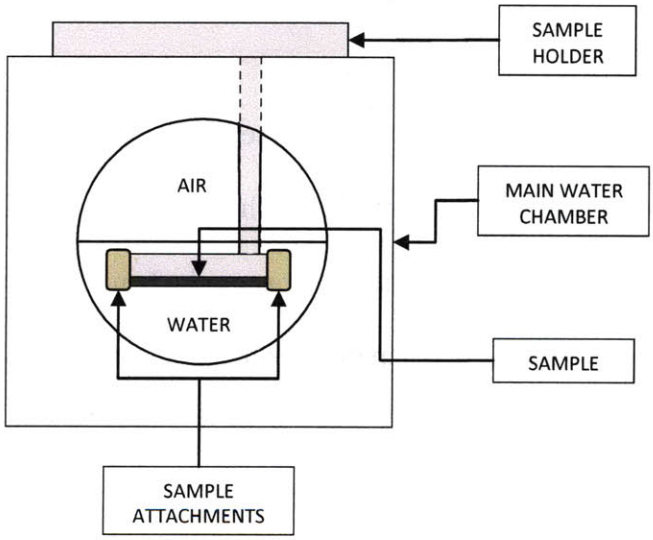

Figure 4.1.3 An illustration of the water chamber that shows the three components: the sample holder, the main water chamber, and the sample attachments. The main water chamber has two windows on opposite sides that allow for light from the fiber optic lamp to backlight the sample so that it can be imaged by the camera on the other side. The top of the main water chamber is open so that it when it is covered with the top of the sample holder, the bottom of the sample holder is in the water chamber. The sample is attached to the bottom of the sample holder with the sample attachments so that a bubble can be trapped underneath and on the sample surface.

The sample fixture was simultaneously lit with ambient overhead lighting and backlit with a brightness-adjustable fiber optic light in the same plane as the camera. The camera had a fixed aperture and shutter speed and therefore the focus could only be adjusted by moving the camera. This also allowed the software to automatically calculate the width of the bubbles and droplets at the surface.

A separate water chamber was attached to the sample stage for the bubble experiments, and is shown in Figure 4.1.3. This water chamber consisted of three components: the main chamber, the sample holder, and the sample attachments. The substrates were attached upside-down to the sample holder with the sample attachments and then the subsystem was placed into the main chamber. The water chamber was filled with deionized water so that the substrate was completely submerged.

Bubbles and droplets were deposited onto the substrate with an automatic dispensing system. Dispens software was used to control both the dispensing rate and dispensed volume deposited with the dispenser. The same method was used when reintaking fluid and gas in addition to dispensing fluid and gas. When dispensing water droplets, a clean plastic pipet tip was used to dispense deionized water from a reservoir. When dispensing air bubbles, a clean metal j-needle was used to dispense ambient air into the water chamber. This j-needle was placed so that the end of the j needle was underneath the substrate, such that escaping air was trapped onto the substrate surface, creating bubbles on the surface that were then measured.

There were two separate measuring techniques: one for measuring the static contact angle and another for measuring the advancing and receding contact angles. The former method is fairly straightforward: a droplet or bubble of finite volume was deposited onto the substrate and then the contact angle measurement was determined using the DropImage software method. For

the latter measurement, a droplet or bubble of finite volume was deposited onto the surface. Then, keeping the needle in contact with the droplet or bubble, a small, finite percentage of the volume was subtracted, and then a larger, finite volume was added and then subtracted again from the droplet or bubble. The first subtraction gave a precursory receding contact angle, then the subsequent addition gave the advancing contact angle and the final subtraction gave the true receding contact angle. Throughout this process, images were captured at a rate of 4 images/second and were then analyzed through the DropImage software.

The surfaces tested included a variety of substrate materials with smooth finishes. These materials were a single crystal silicon substrate with a smooth silicon dioxide surface, an acrylic sample with a mirror-finish surface, a nylon sample with a smooth surface, a silicon substrate with a smooth fluorosilanized surface, and a glass sample with a mirror-finish surface. As for the microtextured surfaces experiments, four samples with different critical dimensions but all with the same silicon substrate and silicon dioxide surfaces were tested. The surface texture for each surface was etched with a photolithography process. As shown in Figure 4.1.4, the critical dimensions were determined to be the height of the posts h, the width of the square posts a and the distance between posts b. The four samples tested are shown along with the calculated R_f and f for each sample in Table 4.1.1.

Table 4.1.1 This table shows the aspect ratios a, b, and h, the roughness coefficient R_f, and the fractional top surface area of the total projected surface area f.

a	b	h	R_f	f
3	3.2	1.5	1.47	0.234
3	3.2	30	10.4	0.234
10	10	100	11.0	0.250
10	10	3.3	1.33	0.250

4.2 Bubble Wetting of Flat Surfaces

For this set of experiments, a volume of 5 μL of deionized water was deposited onto each surface to measure sessile droplet contact angle. The same volume of air was deposited onto each surface when submerged in the water chamber to measure sessile bubble contact angle. All sessile droplet and bubble contact angle measurements were repeated ten times on ten different locations on each surface for a total of one hundred measurements. To measure bubble contact angle hysteresis, a volume of 6 μL of air was deposited onto the surface. The needle was kept in contact with the bubble and 1 μL of air was then drawn back into the needle at a constant volume flow rate of 0.210 μL/second. This step provides a baseline for comparison when determining the advancing contact angle. With the needle still in contact with the bubble, 10 μL of air was added to the bubble at the same constant volume flow rate and then subtracted again.

The important data acquired from each hysteresis experiment image includes the time at which each image was recorded, the width of the droplet at the surface, and the contact angle. These first two variables can be manipulated to find the contact line velocity, v_{cl}

$$v_{cl} = \frac{dw}{2dt}$$

where dw is the change in width between each image capture and dt is the time between each image capture. The factor of two in the denominator is included to reflect that the width is the diameter of the bubble at the surface and v_{cl} is a measure of the change in radius.

A sample of a resulting hysteresis experiment plot is shown in Figure 4.2.1. The advancing contact angle was taken as the average value of the contact angle at the plateau of its upper range and the receding contact angle was taken as the minimum value of the contact angle. Unfortunately, the contact line velocity was similarly noisy in each sample. A total of six hyst eresis experiments were performed on each substrate.

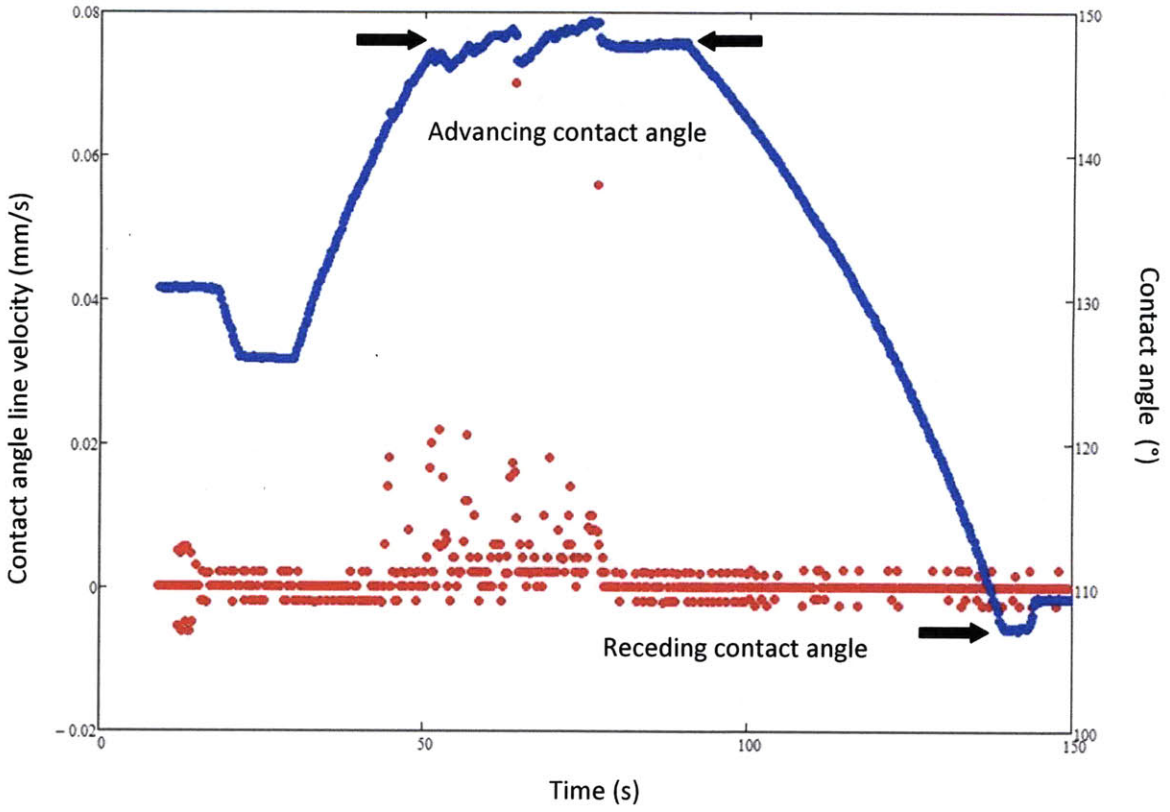

Figure 4.2.1 This plot shows the results for a contact angle hysteresis experiment on nylon. The contact angle hysteresis itself is shown in blue while the contact angle line velocity is shown in red. It is very clear that the contact angle line velocity measurements suffered from noise. The range where the advancing contact angle was averaged is indicated, as well as the minimum that was determined as the receding contact angle.

The complete results from all the flat surface experiments are given in Table 4.2.1 and Figure 4.2.2. To compare the results to the model described in Section 3.3, first the bubble contact angle hysteresis range for each substrate was calculated by subtracting the receding contact angle from the advancing contact angle. The theoretical value of the sessile bubble contact angle using Young's equation was calculated by subtracting the experimentally

determined sessile droplet contact angle from 180 degrees. The difference between the experimental value and the theoretical value of the sessile bubble contact angle was calculated by subtracting the latter from the former. The only substrate that had a negative difference (where the bubble wetted the surface more than Young's equation predicted) was the silicon sample, which exhibited little or no hysteresis. All these results are given in Table 4.2.2 and Figures 4.2.3-4.

Table 4.2.1 Results from contact angle experiments on the five flat materials, where all measurements are in degrees. The values of the uncertainties were calculated using the t-student distribution, which assumes that as the number of measurements approaches infinity, the distribution approaches a Gaussian distribution.

Material	$\theta_{droplet}$	θ	$\theta_{advancing}$	$\theta_{receding}$
Acrylic	70.6±0.7	113.9±1.9	113.9±4.1	93.3±9.1
Fluorosilanized Silicon	97.3±1.7	114.7±5.3	129.0±3.4	83.2±5.8
Glass	62.1±0.9	148.1±9.8	150.5±3.8	111.1±7.9
Nylon	86.2±1.2	139.0±5.8	150.1±3.9	105.1±5.4
Silicon	17.3±0.8	159.9±1.4	162.2±0.7	159.4±0.7

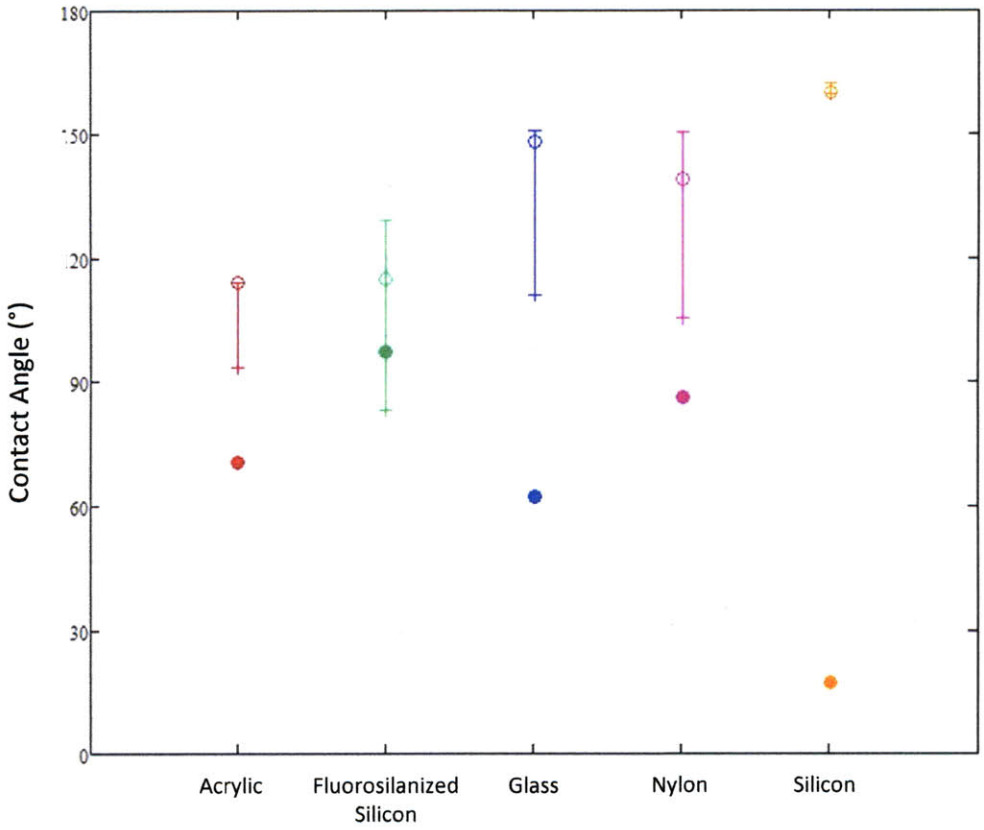

Figure 4.2.2 A comparative plot of the results for the bubble contact angle and droplet contact experiments on flat surfaces. The experimental results for bubble contact angle are represented as open circles. The filled circles show the experimentally determined droplet contact angle. The upper error bar value is the advancing bubble contact angle and the lower error bar value is the receding bubble contact angle.

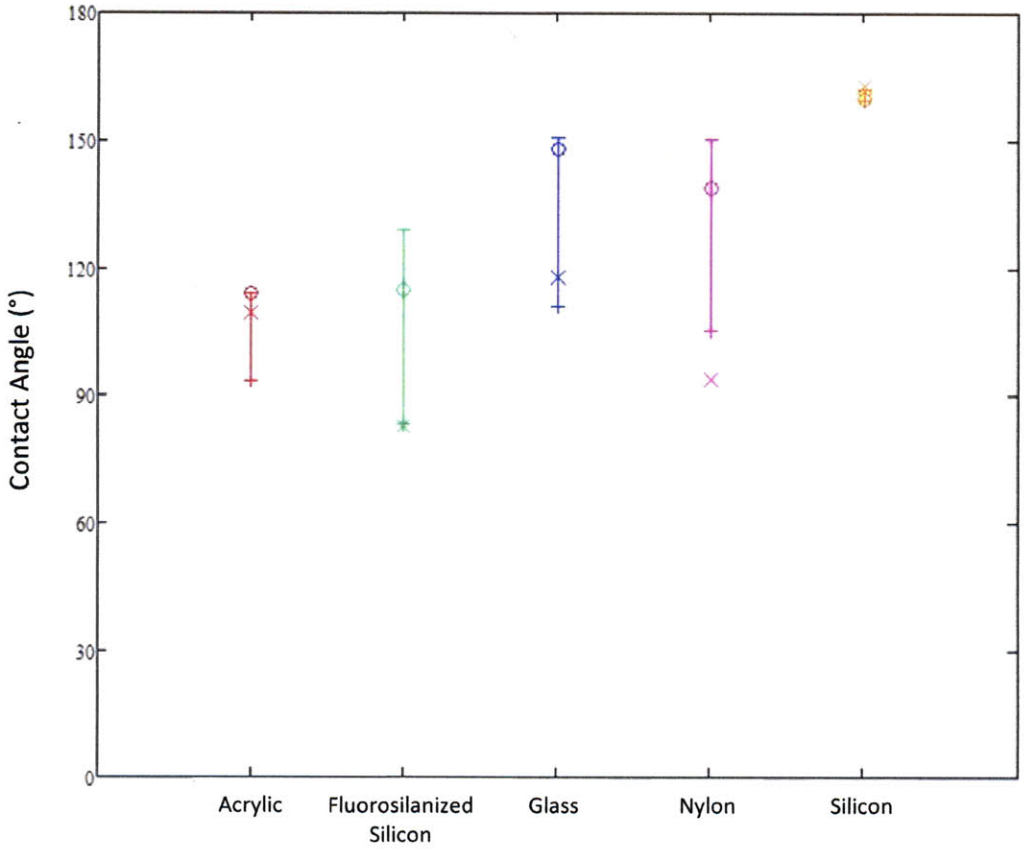

Figure 4.2.3 A comparative plot of the flat surface results for the bubble contact angle experiments and the expected bubble contact angle values based on the droplet contact angle experiments. The experimental results for bubble contact angle are represented as open circles. The X's show the expected bubble contact angle based on the experimentally determined droplet contact angle for each surface. The upper error bar value is the advancing bubble contact angle and the lower error bar value is the receding bubble contact angle.

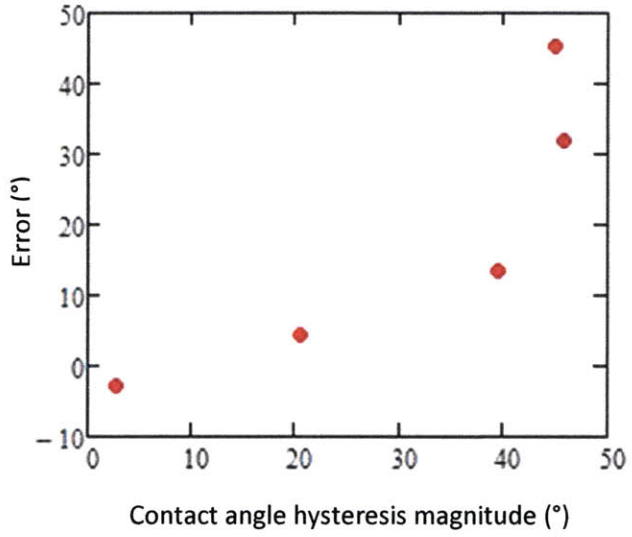

Figure 4.2.4 This plot shows the error between the expected value of the bubble contact angle based on the droplet contact angle on the same surface and the experimentally determined bubble contact angle over the contact angle hysteresis magnitude for each substrate.

To determine whether or not there exists a correction factor that is dependent on the magnitude of the contact angle hysteresis, the error between the expected result from Young's equation and the measured result was tabulated along with the magnitude of the contact angle hysteresis. These results are given in Table 4.2.3. The error was then plotted against the contact angle hysteresis magnitude for each sample. The Pearson's correlation coefficient between the two variables was calculated to be 0.863, a good indicator that the two variables are indeed correlated.

4.3 Bubble Wetting of Textured Surfaces

As for the experiments in Section 4.2, volumes of 5 μL of deionized water and air were deposited onto each surface to measure sessile droplet contact angle and sessile bubble contact

angle, respectively. Again, all sessile droplet and bubble contact angle measurements were repeated ten times on ten different locations on each surface for a total of one hundred measurements. However, the method of measuring bubble contact angle hysteresis changed somewhat. Because the bubbles did not wet the surface well, and because the hysteresis was small for each measurement, a smaller volume was added and subtracted. The first steps are the same: a volume of 6 μL of air was deposited onto the surface and then 1 μL of air was then drawn back into the needle at a constant volume flow rate of 0.210 μL/second while keeping the needle in contact with the bubble. Now instead of 10 μL of air, 3 μL of air was was added to the bubble at the same constant volume flow rate and then subtracted again to make the bubble contact angle hysteresis measurements.

Table 4.3.1 Results from contact angle experiments on the four textured silicon surfaces, where all measurements are in degrees. The values of the uncertainties were calculated using the t-student distribution, which assumes that as the number of measurements approaches infinity, the distribution approaches a Gaussian distribution.

a	b	h	$\theta_{droplet}$	θ	$\theta_{advancing}$	$\theta_{receding}$
3	3.2	1.5	4.2±1.3	169.9±1.2	174.2±2.8	171.6±2.5
3	3.2	30	7.4±0.6	172.0±1.2	174.8±3.2	171.5±2.1
10	10	100	5.7±0.9	173.0±0.6	173.9±2.9	169.0±0.5
10	10	3.3	6.1±1.1	170.5±1.1	175.4±2.1	169.9±1.3

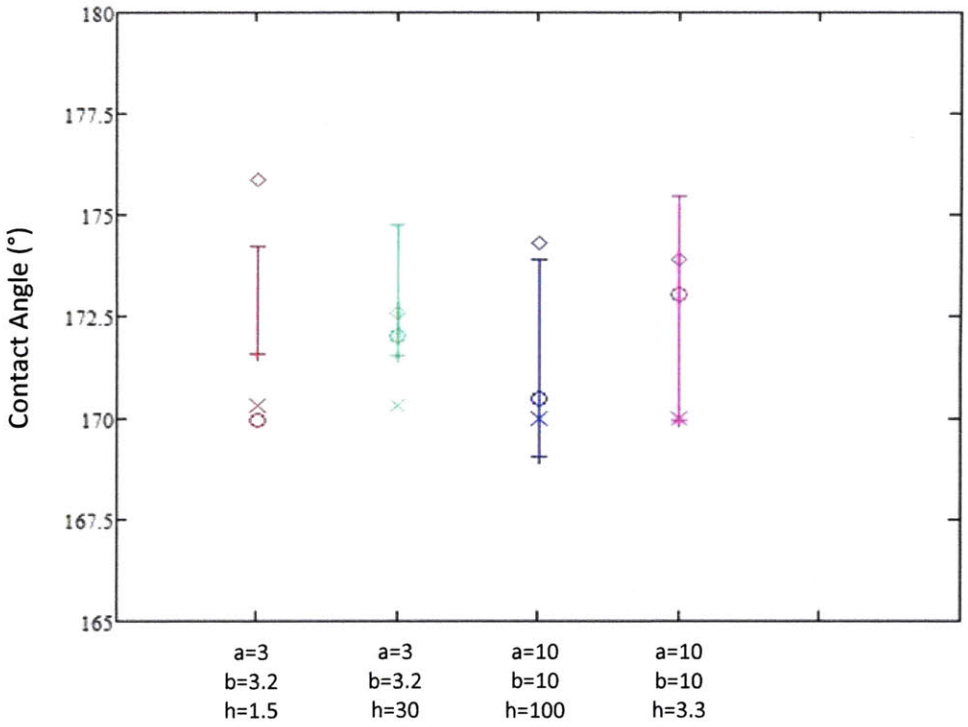

Figure 4.3.1 A comparative plot of the results for the bubble contact angle and the predicted bubble contact angles on the textured surfaces. The experimental results for bubble contact angle are represented as open circles. The X's represent the bubble contact angle prediction from the bubble-based Cassie-Baxter model. The open diamonds represent the bubble contact angle prediction from the droplet-based Wenzel model. The upper error bar value is the advancing bubble contact angle and the lower error bar value is the receding bubble contact angle.

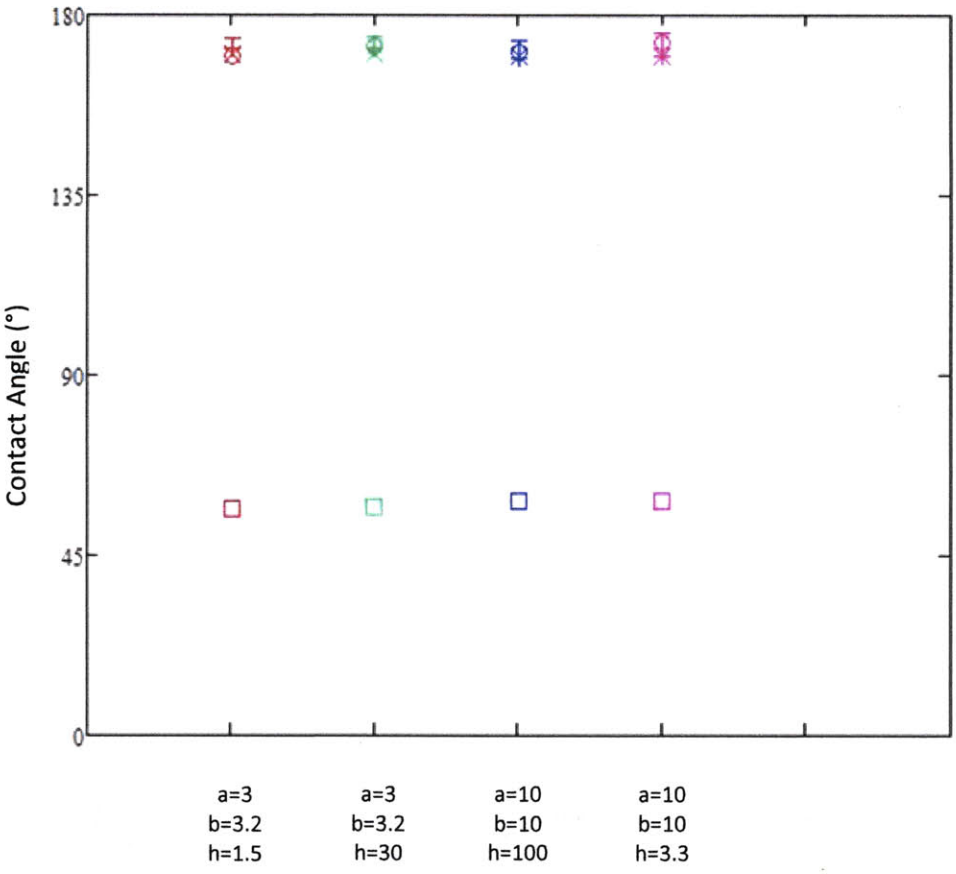

Figure 4.3.2 A comparative plot of the results for the bubble contact angle and the predicted bubble contact angles on the textured surfaces. The experimental results for bubble contact angle are represented as open circles. The X's represent the bubble contact angle prediction from the bubble-based Cassie-Baxter model. The open squaress represent the bubble contact angle prediction from the droplet-based Cassie-Baxter model. The upper error bar value is the advancing bubble contact angle and the lower error bar value is the receding bubble contact angle.

The same data as in Section 4.2 was extracted from each image and used to calculate v_{cl}, and the contact angle in time and plotted and analyzed as before. The results are given in Table 4.3.1 and Figures 4.3.1-2 along with the expected values from the different models given in Equations 2.3.6, 3.2.1, and 3.2.2d. The average error percentage for each model is given in Table 4.3.2. As predicted, the model based on a comparison between a Cassie state bubble on a textured surface and a bubble on a flat surface was most accurate. Second most accurate prediction was from the model based on comparing the bubble contact angle with the measured droplet value on the same surface assuming that both were in the Wenzel state. Least accurate by far was the model based on assuming that both the bubble and droplet were in a Cassie state on the surface.

Table 4.3.2 A comparative table of the average error between the predicted value and the experimentally determined value of the bubble contact angle for each of the discussed prediction methods.

Model	**Flat Bubble**	**Wenzel Droplet**	**Cassie Droplet**
Average Error Percentage	0.8	1.7	66.2

The wide gap in accuracy between the Wenzel droplet method and the Cassie droplet method could be in that the measured droplet contact angles that each model used in its calculations was indeed in the Wenzel state. Furthermore, because the bubble contact angle was already very large, an incorrect roughness factor is more forgiving, though it does result in the overestimation that can be seen in Figure 4.3.1.

4.4 Chapter Summary

Sessile droplet contact angle and trapped bubble contact angle and bubble contact angle hysteresis measurements were taken for smooth acrylic, fluorosilanized silicon, glass, nylon and silicon and for four silicon samples with different surface textures. For the smooth surfaces, a correlation with Pearson's coefficient of 0.863 was determined to exist for the magnitude of the contact angle hysteresis and the error between the expected value of the contact angle based on Young's equation and the experimentally determined value. For the textured surfaces, the experiments bore out the prediction that the best model for predicting the contact angle of a trapped bubble on a textured surface is based on the contact angle of a trapped bubble on the smooth surface.

Chapter 5

Conclusion

This thesis studies bubble wetting on surfaces and current methods for predicting bubble wetting. Although most current methods assume that a trapped bubble can be analyzed exactly as if it were a droplet, the analysis performed in this paper indicated that two factors could prove to affect bubbles differently than droplets: gravitational effects and disjoining pressure effects. Current methods for analyzing droplets on textured surfaces were also explored, and it was predicted that the best method for predicting the contact angle of a bubble on a textured surface would be based on the contact angle of a bubble on a flat surface of the same material.

Contact angle measurements of bubbles and droplets on five different flat surfaces and four different textured silicon samples were performed. Using the flat surface data, a strong correlation with a Pearson's correlation coefficient of 0.863 was observed between the contact angle hysteresis and the error for the contact angle value predicted using current methods. Because contact angle hysteresis is related to disjoining pressure, these results are a good indicator that disjoining pressure affects bubbles differently than droplets and in a significant way. For the textured silicon samples, little hysteresis was observed, so no disjoining pressure analysis was made. Instead, results were compared to values expected from the Cassie-Baxter model based on droplet results for the same textured surface, values expected from the Wenzel model based on droplet results for the same textured surface, and values expected from the

Cassie-Baxter model based on bubble results on the flat surface of the same material. As expected, the Cassie-Baxter model based on bubble results on the flat silicon dioxide surface was most accurate, with the Wenzel model being the next most accurate and the droplet Cassie-Baxter model being by far the least accurate. These secondary results reflect that the droplet was much more in a Wenzel state than in a Cassie-Baxter state.

Because of limited time and resources, a study of gravitational effects was not entirely possible. The volume of air dispensed by the dispenser could not be fully trusted to be as accurate as the volume of water dispersed by the dispenser because of the pressure differential inherent in creating bubbles. In order to have truly accurate volume measurements, special software would have been necessary. Further experiments could focus on gravitational effects, and could even test bubbles and droplets of different volumes.

Additional experiments could also include performing these same experiments on textured surfaces on materials with higher hysteresis to test whether or not the disjoining pressure effects are significantly affected with surface texture. Another possible addition would be to also test the contact angle hysteresis of the droplets and see how these results compare to the bubble contact angle hysteresis.

Bibliography

[1] Bhushan, Bharat and Michael Nosonovsky. *Multiscale Dissipative Mechanisms and Hierarchical Surfaces.* New York, NY: Springer-Verlag Berlin Heidelberg, 2008: 74+.

[2] Cini, Renato, Augusta Ficalbi, and Giuseppe Loglio. "Temperature Dependence of the Surface Tension of Water by the Equilibrium Ring Method." *Journal of Colloid and Interface Science* Nov, 1972: 289-292.

[3] Clarence A. Miller and P. Neogi. *Interfacial Phenomena: Equilibrium and Dynamic Effects.* Boca Raton, FL: CRC Press, 2008: 6+.

[4] De Gennes, Pierre-Gilles, Francoise Brochard-Wyart, and David Quere. *Capillarity and Wetting Phenomena: Drops, Bubbles, Pearls, Waves*. Trans. Axel Reisinger. New York, NY: Springer Science+Business Media, 2004: 2+.

[5] "DNA Side | Mathies Lab." *Mathies Lab | University of California, Berkeley*. Web. 05 May 2010. <http://endlesstrek.com/node/1>.

[6] Feng, Lin et.al. "Petal Effect: A Superhydrophobic State with High Adhesive Force." *Langmuir* 08 Nov, 2008: 4115-4117.

[7] Radke, Clayton J., Victor M. Starov and Manuel G. Velarde. *Wetting and Spreading Dynamics.* Boca Raton, FL: CRC Press, 2008: 3+.

[8] Salmeron, Miquel and Lei Xu. "Scanning Polarization Force Microscopy Study of the Condensation and Wetting Properties of Glycerol on Mica." *Journal of Physical Chemistry* 23 Jun, 1998: 7212-7214.

[9] Whitesides, George M. "The Origins and the Future of Microfluidics, *Nature* 27 Jul. 2006: 368+.